Ultrathin PdAg single-crystalline nanowires enhance ethanol oxidation electrocatalysis

Hao Lv[a], Yang Wang[a], Aaron Lopes[b], Dongdong Xu[a,*], Ben Liu[a,*]

[a] *Jiangsu Key Laboratory of New Power Batteries, Jiangsu Collaborative Innovation Center of Biomedical Functional Materials, School of Chemistry and Materials Science, Nanjing Normal University, Nanjing 210023, China*
[b] *Department of Chemical Engineering, Massachusetts Institute of Technology, Cambridge, MA 02139, United States*
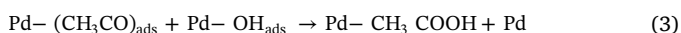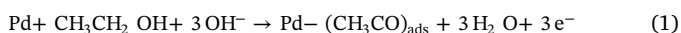
ARTICLE INFO

ABSTRACT

Rational design and synthesis of highly efficient nanocatalysts towards electrochemical ethanol oxidation reaction (EOR) are of great importance for practical applications in direct ethanol fuel cells. Nanoengineering the nanostructures and compositions of EOR electrocatalysts has been of significnat interest because these paratmeters can enhance electrocatalytic kinetics and performance in the EOR. This article reports a synergistic EOR catalyst with remarkably enhanced electrochemical performance based on 3-nm-thick bimetallic PdAg single-crystalline nanowires. Kinetically stable yet thermodynamically unfavorable ultrathin PdAg single-crystalline nanowires (sNWs) are epitaxially grown *in situ* along nanoconfined hexagonal mesophases directly self-assembled by amphiphilic surfactants of dioctadecyldimethylammonium chloride under optimal synthetic condtions in aqueous solution. Due to the ultrathin and ultralong nanostructure, single-crystalline feature with a high density of low-coordinate atomic steps, high Pd utilization efficiency, and incorporation of more oxophilic Ag with Pd, PdAg sNWs show enhanced mass activity of 2.84 A mg_{Pd}^{-1} and stability (retained 43% after 2500 cycles) in the EOR. The kinetic studies reveal that significant enhancement in EOR performance can be ascribed to the synergic electronic and bifunctional effects of ultrathin PdAg sNWs.

1. Introduction

Direct alcohol fuel cell (DAFC) is considered to be one of the most promising energy conversion devices, based on high energy conversion efficiency and good environmental sustainability. Out of all DAFCs commercially available, direct ethanol fuel cells (DEFCs) have recently received tremendous attention, because ethanol possesses a high theoretical energy density in addition to being is less-toxic, renewable, and easy to store and transport [1–3]. Precious metal palladium (Pd) has been considered as one of the most efficient anode catalysts of the DEFCs towards electrochemical ethanol oxidation reaction (EOR) in alkaline solution [4,5]. It is widely accepted that EOR proceeds on Pd catalysts according to the following mechanisms [4,6,7]:

$$Pd + CH_3CH_2OH + 3OH^- \rightarrow Pd-(CH_3CO)_{ads} + 3H_2O + 3e^- \quad (1)$$

$$Pd + OH^- \rightarrow Pd-OH_{ads} + e^- \quad (2)$$

$$Pd-(CH_3CO)_{ads} + Pd-OH_{ads} \rightarrow Pd-CH_3COOH + Pd \quad (3)$$

$$Pd-CH_3COOH + OH^- \rightarrow Pd + CH_3COO^- + H_2O \quad (4)$$

The rate-determining step of electrochemical EOR is the oxidation/removal of poisoning carbonaceous intermediates on Pd (Pd-$(CH_3CO)_{ads}$) by adsorbed OH (OH_{ads}) (Eq. (3)). An effective solution to enhance the electrocatalytic activity while decreasing the usage of precious metals is alloying Pd with less-expensive metals (e.g. Ag and Au) into bimetallic counterparts. Incorporation of secondary oxophilic metals facilitates the formation of OH_{ads} and thus accelerates the reaction/removal between $M-OH_{ads}$ and Pd-$(CH_3CO)_{ads}$, and eventually boosts the electrochemical EOR performances kinetically (bifunctional effect) [8–11]. Meanwhile, the electronic and ligand effects of bimetallic alloys contribute also to the enhanced electrochemical activity by weakening the adsorption affinity of Pd-$(CH_3CO)_{ads}$ based on the well-known D-band theory [12–15]. However, the high surface energy of zero-dimensional (0D) Pd-based nanoalloys inevitably causes agglomeration into larger particles due to inherent dissolution and Ostwald ripening processes [5], which severely decrease the surface area and significantly degrade the activity during the electrocatalysis.

Increasing the dimensions and crystallinities of the nanocatalysts has been recognized as alternative methods to boost electrocatalytic performances [16–23]. Breaking the symmetry of face-centered cubic

---

* Corresponding authors.
  E-mail addresses: ddxu@njnu.edu.cn (D. Xu), ben.liu@njnu.edu.cn (B. Liu).

(fcc) Pd-based nanoalloys into anisotropic 1D nanowires (NWs) obviously increases the utilization efficiency of surface Pd atoms and strengthens the physical contraction with contiguous carbon supports/electrodes [24]. Such structural evolution not only decreases the usage of precious Pd, but also enhances the self-stability of 1D Pd-based catalysts [25–27]. More importantly, anisotropic NWs possess single-crystalline features which would further facilitate electron/mass transformation and the adsorption/desorption of the reactant intermediates, and thus accelerate the reaction kinetics during the electrocatalysis [25,26,28–32]. In addition, 1D NWs with ultrathin diameter (1–3 nm) would further enhance the electrocatalytic activity by a surface contraction effect [33]. Therefore, we rationally anticipate that a highly active and stable EOR electrocatalyst can be fabricated by synergistically combining the multiple advantages of bimetallic Pd-based nanoalloys and ultrathin 1D single-crystalline NWs (sNWs).

In this manuscript, we present a powerful one-step solution-phase synthetic methodology to controllably prepare thermodynamically unfavorable ultrathin 1D bimetallic PdAg sNWs with tailorable composition ratios using a surfactant-directing approach. Although ultrathin 1D Rh-doped Pt sNWs (< 50 nm in length and < 13 at% for Rh) have been formed by an oil-phase high-temperature method [26], the scale-up synthesis of 1D bimetallic PdAg sNWs with the diameters of < 3 nm and the lengths of > 100 nm is achieved in one step in an ambient aqueous solution. By rationally adjusting the reaction kinetics and optimizing synthetic conditions, the formation mechanism of ultrathin PdAg NWs is also unveiled. Thanks to synergistically structural and compositional advantages, the resultant ultrathin PdAg sNWs exhibit significantly enhanced electrocatalytic activity and stability towards electrochemical EOR in alkaline solution, with respect to ultrathin PdAg polycrystalline NWs (pNWs), 0D PdAg nanoparticles (NPs), Pd sNWs, and commercial PdNPs. The origin of enhancement in electrocatalytic EOR performances is finally elucidated by reaction kinetics/thermodynamics and CO anti-poisoning investigations on ultrathin PdAg sNWs.

2. Experimental section

2.1. Chemicals

Palladium(II) chloride ($PdCl_2$, 99.9 wt%), silver nitrate ($AgNO_3$), commercial palladium nanoparticles (PdNPs), polyvinylpyrrolidone (PVP), dioctadecyldimethylammonium chloride (DODAC), cetyltrimethylammonium chloride (CTAC), sodium citrate, sodium borohydride ($NaBH_4$) and L-ascorbic acid (AA) were purchased from Alfa Aesar. Hydrochloric acid (HCl) and ethanol were obtained from Sinopharm Chemical Reagent Co. Ltd. (Shanghai). Nafion solution was purchased from Sigma Aldrich. To prepare 10 mM H_2PdCl_4 solution, 0.36 g of palladium (II) chloride was dissolved in 20 mL of 0.2 M HCl solution and further diluted to 200 mL with deionized H_2O. All the reagents are of analytical reagent grade and used without further purification. Deionized H_2O with the resistivity of 18.25 mΩ was used in all experiments.

2.2. Synthesis of ultrathin PdAg sNWs

Ultrathin single-crystalline PdAg bimetallic NWs were synthesized by a solution-phase route using DODAC as the surfactant template, H_2PdCl_4 and $AgNO_3$ as metal precursors and AA as the reducing agent at 95 °C. Taking ultrathin Pd_2Ag_1 nanowires as an example, 0.667 mL of H_2PdCl_4 (10 mM) and 0.334 mL of $AgNO_3$ solution (10 mM) were mixed with 10 mL of 5 mM DODAC solution. The solution was further kept at 95 °C to drive the co-assembly of DODAC/metal precursors into hexagonal mesophase. Then, 1.0 mL of freshly prepared AA (0.3 M) was rapidly injected into the above solution, following the quick color change of the solution from pink to dark brown. After an additional 30 min at 95 °C, the product was collected by centrifugation and washed several times with ethanol/H_2O, and then freeze dried at −60 °C

before use. Similarly, ultrathin PdAg bimetallic nanowires with different molar ratios were synthesized using similar procedures by simply changing the feed ratios of Pd to Ag. In addition, the concentrations of surfactant (DODAC), reaction temperatures, the kinds of surfactants, and reducing agents were also tuned to control the nanostructures of resultant bimetallic PdAg nanoalloys using similar procedures.

2.3. Electrochemical EOR measurements

Electrocatalytic EOR tests were performed on the CHI 660E electrochemical analyzer at 25 °C A three-electrodes system was used for all electrochemical tests, in which glassy carbon electrode (GCE, 0.07065 cm^2) was used as the working electrode, a carbon rod was the counter electrode, and a Ag/AgCl electrode was the reference electrode. An ink of the catalysts was prepared by mixing 1 mg of catalysts, 4 mg of Vulcan XC-72 carbon, 1.5 mL of ethanol and 0.5 mL of H_2O. After sonicating for 0.5 h, 50 μL of Nafion solution (5 wt% in alcohol and H_2O) was added and further sonicated for 0.5 h. Then, 6 μL of above-prepared ink solution (3 μg of the catalyst) was casted on the GCE electrode and dried at 40 °C before testing. CVs were used to evaluate the electrochemical surface areas and activities of different nanocatalysts. The electrolyte solution was initially purged with N_2 for 30 min before testing. Electrochemical active surface areas (ECSAs) of the Pd-based catalysts were calculated from CVs in the area of the PdO reduction peak, while CO active areas were obtained from the area of the oxidation peak of CO_{ads}. ΔE_a values of four catalysts were calculated based on the Arrhenius equation as follows:

$$I = Ae^{-\frac{\triangle E_a}{RT}}$$

where I is the current at a specific potential, R is the gas content (8.315 J mol^{-1} K^{-1}), T is the test temperature in K and ΔE_a is the apparent activation energy at a specific potential.

2.4. Structural and compositional characterizations

High-resolution TEM studies were carried out using a JEOL 2010 transmission electron microscope with an accelerating voltage of 200 kV. Images were recorded with a Gatan CCD camera (resolution 4000 × 2700 pixels, pixel size 9 x 9 μm). HAAD-STEM was taken on an FEI Talos F200X apparatus at an accelerating voltage of 200 kV, which is equipped with STEM and EDS detectors for elemental mapping analysis. TEM and STEM samples were prepared by dropping a suspension of the samples on a carbon coated copper grid (300 mesh). XRD patterns were recorded on powder samples using a D/max 2500 V L/PC diffractometer (Japan) equipped with graphite-monochromatized Cu Kα radiation in *2θ* ranging from 30° to 85°. Related working voltages and currents were 40 kV and 100 mA, respectively. XPS were performed on a scanning X-ray microprobe (Thermo ESCALAB 250Xi) that uses Al Kα radiation. The binding energy of the C 1 s peak (284.8 eV) was employed as a standard to calibrate the binding energies of other elements.

3. Results and discussion

3.1. Structural characterizations and formation mechanism

Ultrathin bimetallic PdAg sNWs were synthesized by a one-step solution-phase approach, in which H_2PdCl_4 and $AgNO_3$ were used as the metal co-precursors, dioctadecyldimethylammonium chloride (DODAC) as the surfactant template, and ascorbic acid (AA) as the reducing agent at 95 °C (see Experimental for details). Ultrathin 1D PdAg sNWs with a compositional ratio of 2/1 (defined as Pd_2Ag_1) were first characterized thoroughly by electron microscopy to reveal the nanostructure and crystallinity, since this system exhibited the best electrocatalytic EOR activity (see below). As shown in Fig. 1a, low-
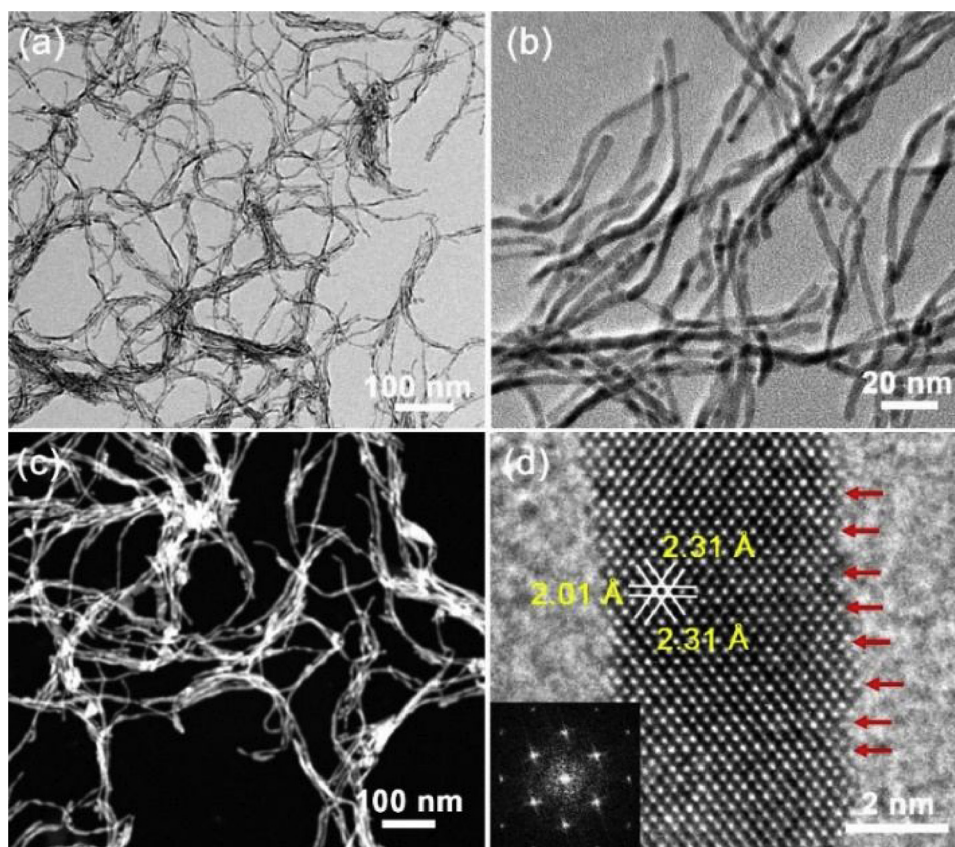
Fig. 1. (a, b) Low-magnification TEM, (c) HAADF-STEM, (d) high-resolution TEM images and corresponding FD pattern (inset in (d)) of ultrathin Pd_2Ag_1 sNWs.

magnification transition electron microscopy (TEM) image showed ultralong 1D NW nanostructure with a high uniformity and purity (see more TEM images in Figure S1). The length of ultralong NWs was in the range of 100–1000 nm. High-magnification TEM images revealed that the NWs were ultrathin with an average diameter of 2.9 nm (Fig. 1b). The nanostructure of ultralong and ultrathin NWs was also confirmed by high-angle annular dark-field scanning TEM (HAADF-STEM) (Fig. 1c). High-resolution TEM image of an individual NW displayed two sets of lattice fringes with the *d*-spacings of 2.31 and 2.01 Å, respectively, which were ascribed to (111) and (200) planes of face-centered cubic (fcc) PdAg alloys (Fig. 1d). The corresponded Fourier transform (FT) pattern further confirmed the [110] crystalline observation direction along the NW. Meanwhile, slightly uneven and undercoordinated surface atoms with clear lattice boundaries were observed in bimetallic PdAg sNWs from high-resolution TEM images, thus indicating more exposed active sites for the electrocatalysis.

The single-crystalline feature of ultrathin Pd_2Ag_1 sNWs was further investigated by detailed high-resolution TEM observations (Fig. 2). An individual ultralong NW (not straight) exhibited obvious selected-area electron diffraction (SAED) spots (Fig. 2b), in which only a single set of signals suggested the single-crystalline nature. We further investigated the crystalline structures by identifying three parts in this NW (Fig. 2c–e). Both high-resolution TEM and corresponding FT patterns of three different domains exhibited identical *d*-spacings and orientations of the lattice fringes; therefore, this further indicating that the ultrathin NWs are single-crystalline in structure.

The elemental distributions of ultrathin Pd_2Ag_1 sNWs were further disclosed by STEM dispersive X-ray (EDX) elemental mappings and corresponded line scan analysis. As shown in Fig. 3a, the Pd and Ag elements were homogeneously distributed throughout sNWs, showing the successful formation of bimetallic PdAg alloys, rather than phase-separated counterparts. STEM line scan profiles of three PdAg sNWs arranged in parallel further indicated the formation of bimetallic PdAg

NWs (Fig. 3b). The actual molar ratio of Pd to Ag was 65.8:34.2 (Fig. 3d), almost identical to the feed ratio (2:1). X-ray photoelectron spectroscopy (XPS) survey also indicated the ultrathin NWs were composed of Pd and Ag elements with molar ratios of ~2:1 (Fig. 3c). The high-resolution XPS analysis was further assessed to reveal the electronic states. Obviously, the incorporation of Ag with Pd into bimetallic PdAg alloys caused a ~0.21 eV shift positively in binding energy of Pd 3d (Figure S2), which corresponded to the upshift of core levels in the Fermi level of Pd [34]. This result indicates that the ᴅ-band center of Pd shifted upwards due to the strong electronic interaction of Pd/Ag within bimetallic PdAg nanoalloys [8,11]. Similarly, the slightly higher Ag 3d XPS peaks were also seen for both bimetallic Pd_2Ag_1 sNWs (Figure S3), than those observed for monometallic Ag nanocrystals [35,36], also suggesting the formation of bimetallic PdAg alloys. Finally, the successful synthesis of bimetallic PdAg alloys was confirmed by wide-angle X-ray diffraction (XRD) (Fig. 3e). Only a single set of XRD peaks, which were located in between standard peaks of pure Pd and Ag, provided the direct evidence of the formation of fcc PdAg alloys. The microscopic and spectroscopic characterization studies shown above, therefore, suggest the first successful synthesis of sub-3 nm-thick 1D bimetallic PdAg sNWs.

Our one-step synthetic method in aqueous solution was reactively quick (~30 min), scalable to gram-scale, and reproducible. The chemical compositions and resultant nanostructures of bimetallic PdAg alloys were rationally controlled by tuning the feed ratios of Pd/Ag, changing the surfactants and reducing agents, and controlling the reaction temperature. For example, chemical composition ratios of PdAg alloys can be easily tuned by tailoring the initial feed ratios of metal precursors. As shown in Fig. 4a–c, when the molar ratios of Pd in PdAg alloys were higher than 66.7%, the resultant products were composed of ultrathin 1D sNWs, structurally the same as Pd_2Ag_1 sNWs (see Figure S4 for more details). However, incorporating more than 50 at% of Ag (for example, Pd_1Ag_1) resulted in the formation of 1D pNWs with the thicker
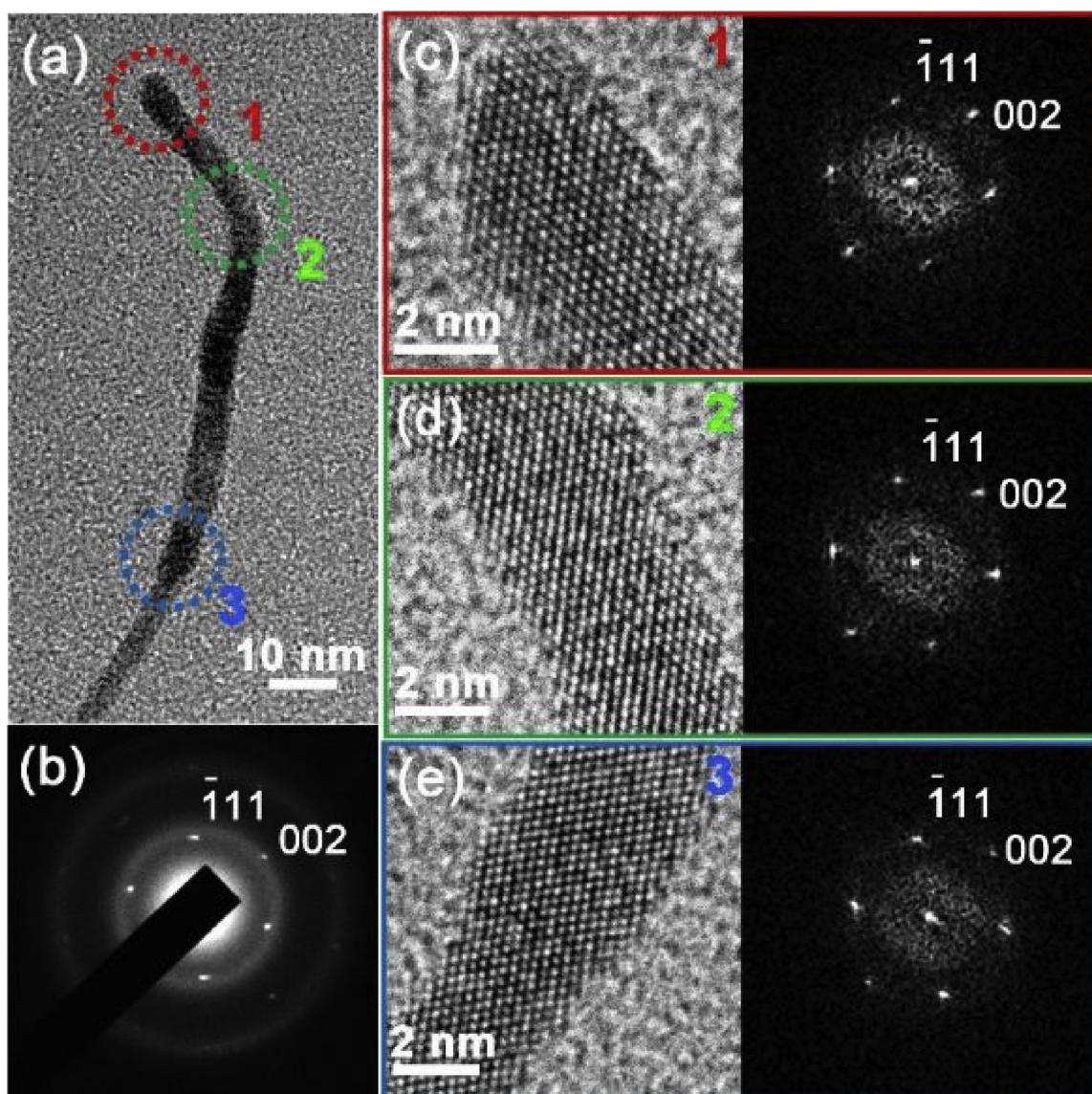
Fig. 2. (a) Low-magnification TEM and (b) SAED pattern of ultrathin Pd_2Ag_1 sNWs, and (c–e) high-resolution TEM images and corresponded FDs patterns labeled in (a).

diameters and the shorter lengths, which evenly packed into larger bundles (Fig. 4d). This possibly attributed to the lower nucleation energy barrier and the quicker nucleation rate of Ag nanocrystals, compared to $PdCl_4^{2-}$/Pd [37,38], which accelerated the crystallization of bimetallic PdAg nanoalloys. Furthermore, the higher Ag content in Pd_1Ag_3 nanostructures (NSs) gave rise to the formation of NP aggregates with irregular morphology (Fig. 4e), indicating that the reduction of Ag^+ destroyed *p6mm* micelle structure of DODAC, which could be also implied by irregular, thermodynamically stable large NPs or nanorods for pure Ag NSs (Fig. 4f).

Structural observations corroborated that the formation of kinetically stable but thermodynamically unfavorable ultrathin 1D bimetallic PdAg sNWs was kinetically achieved by the epitaxial growth of PdAg nanocrystals along the surfactant template. The surfactant of DODAC with two hydrophobic tails and one hydrophilic quaternary head co-assembled with metal precursors into columnar mesophases in an aqueous solution [39], which further nanoconfined *in-situ* epitaxial growth of bimetallic PdAg nanocrystals into ultrathin 1D sNWs under optimal reaction conditions. Meanwhile, both quaternary head and counter Cl^- ion in DODAC were responsible for the stabilization of (110) facets of PdAg nanocrystals due to surface passivation by DODAC,

and thus blocking the crystalline growth of ultrathin PdAg sNWs along [110] direction. The same growth mechanism has also been observed in 2D PdAg nanodendrites [8], dodecahedral PdAu [40], and $PtCu_3$ nanocrystals previously [41].

We emphasized that both reduction kinetics (the rate of the nucleation and growth of PdAg nanocrystals) and assembled columnar mesophases (the species of surfactants and reaction conditions) played critical roles in controlling resultant nanostructures and uniformity of ultrathin PdAg sNWs. To further reveal the formation mechanism of ultrathin PdAg sNWs, more control experiments were carried out. First, the reducing agents with different reduction rates were investigated in the synthesis. As shown in Fig. 5a, sodium citrate as reducing agent rendered the resulted PdAg NSs into spherical NPs, indicating the slower reduction rate facilitated the formation of thermodynamically stable nanostructures, even suppressing the nanoconfinement effect of DODAC. By contrast, the quicker reducing rate resulted in bimetallic PdAg alloys with 1D nanostructures. The mixtures of the NPs and NWs were obtained using formic acid as the reducing agent (Fig. 5b), while worm-like NWs with polycrystalline feature and 2-nm thickness (pNWs) were grown for the stronger reducing agent of sodium borohydride (Fig. 5c, see Figure S5 for structural characterizations). These results
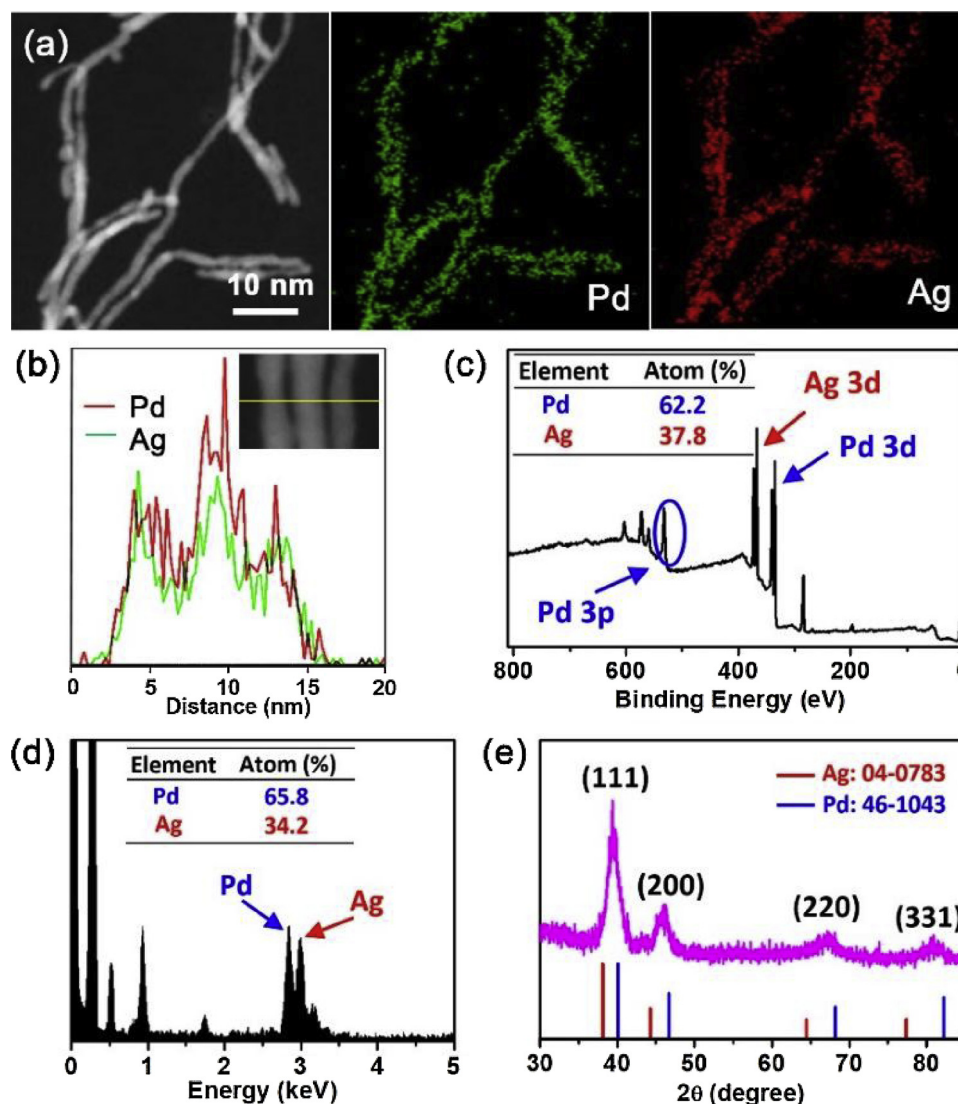
Fig. 3. (a) STEM mappings, (b) corresponded line scans, (c) XPS survey, (d) EDX, and (e) wide-angle XRD pattern of ultrathin Pd$_2$Ag$_1$ sNWs.

indicate that AA as the reducing agent with moderate reduction kinetics was critical for the formation of ultrathin PdAg sNWs.

Second, we investigated the effect of the surfactants, and found that only amphiphilic DODAC with two hydrophilic tails as the structure-directing agent can drive the formation of ultrathin PdAg sNWs in current conditions. Only larger thermodynamically stable irregular NPs and aggregates were obtained in the absence of the surfactant (Fig. 5d). By contrast, using conventional surfactant of cetyltrimethylammonium chloride (CTAC) as the template, slightly smaller NPs (10–20 nm) were synthesized (Fig. 5e). This was possibly ascribed to the insufficient nanoconfinement effect of the surfactant during the crystalline nucleation, similar to those synthesized with the higher Ag content. Polyvinylpyrrolidone (PVP) was also used as the co-surfactant. Because of the strong coordination effect of PVP that changed the binding behaviors of DODAC with metal precursors, the resultant PdAg alloys were structurally composed of NPs and NWs (Fig. 5f). This further highlights the importance of DODAC as the surfactant template for forming columnar mesophases and nanoconfining the crystalline growth of bimetallic PdAg sNWs.

Third, the reaction conditions, which were highly sensitive to the assembled mesophases of DODAC [42,43], were studied carefully. As shown in Fig. 5g–i, when the reaction temperature is lower than 60 °C, 2D PdAg nanosheets or mesoporous nanospheres with significant

impurities were observed. Only reaction temperatures higher than 80 °C produced ultrathin NWs, although small amount of NPs were also seen in the reaction temperature lower than 90 °C (see Figure S6 for more details). The results imply that optimal reaction temperatures were critically important for the formation of ultrathin PdAg sNWs. Similarly, only maintaining the concentration of DODAC in the range of 2.5–5 mM, ultrathin and ultralong PdAg sNWs can be achieved (Figure S7).

3.2. Electrocatalytic EOR performance

Thanks to the anisotropic 3-nm-thick 1D nanostructure, single-crystalline feature with a high density of low-coordinate atomic steps, high utilization efficiency of Pd atoms, and bimetallic PdAg compositions, we deduced that ultrathin PdAg sNWs would synergistically hold excellent performance for electrochemical EOR. We first investigated catalytic activities of bimetallic Pd$_2$Ag$_1$ alloys with different crystalline structures (Pd$_2$Ag$_1$ sNWs (Figs. 1–3), Pd$_2$Ag$_1$ pNWs (Fig. 5c), and Pd$_2$Ag$_1$ NPs (Fig. 5a)) in electrocatalytic EOR, and commercial Pd NPs were also tested as a control. Fig. 6a displayed the cyclic voltammo-grams (CVs) of different Pd-based nanocatalysts collected in N$_2$-saturated 1.0 M KOH solution with a scan rate of 50 mV s^{-1} at 25 °C. The typical reduction peaks in the range of -0.4 and -0.2 V (vs SCE) for all
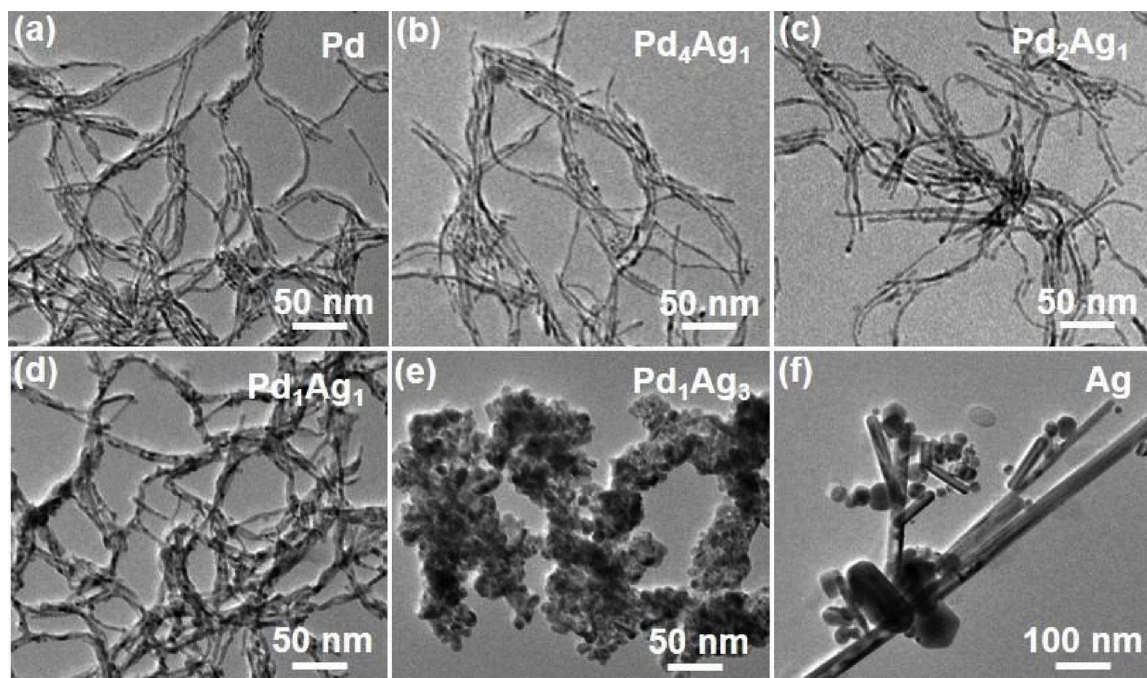
Fig. 4. TEM images of the as-resulted products synthesized with different feed ratio of Pd/Ag of (a) 100:0, (b) 80:20, (c) 66.7:33.3, (d) 50:50, (e) 25:75, and (f) 0:100.

catalysts were observed from reverse scans, which were ascribed to the reduction peaks of PdO [9,11]. The lowest reduction peak potential of -0.36 V was seen for Pd_2Ag_1 sNWs, which gradually increased to -0.35 V for Pd_2Ag_1 pNWs, -0.33 V for Pd_2Ag_1 NPs, and -0.28 V for commercial PdNPs, respectively. The lower reduction peak of PdO may be responsible for the easier reduction of PdO and enhanced activity. Electrochemical active surface areas (ECSAs) were further calculated from CVs in the area of the reduction peak of PdO. Obviously, Pd_2Ag_1 sNWs with single-crystalline feature and high density of low-coordinate atomic steps exhibited the largest ECSA of 25.9 m^2 g_{Pd}^{-1} (Figure S8). By contrast, the ECSA values of commercial PdNPs, Pd_2Ag_1 NPs and pNWs were 11.5, 14.8, 20.8 m^2 g_{Pd}^{-1}, respectively.

Electrocatalytic EOR activities of the above four catalysts were shown in Fig. 6b, which were obtained in 1.0 M ethanol and 1.0 M KOH solution at a scan rate of 50 mV s^{-1}. Two characteristic oxidation peaks, in which the peak in the forward scan was associated with ethanol oxidation and the one in the reverse scan originated from further oxidation or removal of poisoning carbonaceous intermediates, were observed from CV curves. Mass peak current densities (normalized to the amount of Pd) of bimetallic Pd_2Ag_1 sNWs, pNWs and NPs, and commerical Pd NPs were 2.84, 2.32, 1.90, and 0.92 A mg_{Pd}^{-1}, respectively (Fig. 6c). The highest mass activity was achieved by ultrathin Pd_2Ag_1 sNWs, which was 1.20 and 1.47 times higher than Pd_2Ag_1 pNWs and NPs, and 3.03 times higher than commercial Pd NPs. Similarly, the highest specific activity of 11.2 mA cm_{Pd}^{-2} was also achieved for bimetallic Pd_2Ag_1 sNWs. 1D ultrathin PdAg sNWs with single-crystalline feature and high density of low-coordinate atomic steps effectively improved the utilization of Pd and enhanced activity in electrocatalytic EOR. Meanwhile, a low onset potential of -0.78 V was seen for ultrathin Pd_2Ag_1 sNWs, which exhibited a negative shift of ~ 65 mV for Pd_2Ag_1 pNWs, 100 mV for Pd_2Ag_1 NPs, and 140 mV for Pd NPs, respectively (Fig. 6d). This indicates that single-crystalline NWs can intrinsically decrease the onset potential for the EOR. Similarly, the largest Tafel plot was observed for ultrathin Pd_2Ag_1 sNWs (Figure S9), identifying the faster kinetic rate in electrochemical EOR. The enhanced electrocatalytic kinetics of ultrathin Pd_2Ag_1 pNWs was further indicated by changing scan rates, concentrations of ethanol and KOH (Figure S10a-c). Furthermore, a low activation energy (ΔE_a) value of 19.0 kJ mol^{-1} was obtained for ultrathin Pd_2Ag_1 sNWs (Figure S10d), thus suggesting

a small reaction energy barrier and high intrinsic EOR activity [44,45].

CO anti-poisoning experiments were also carried out to clarify the enhanced EOR performance of ultrathin Pd_2Ag_1 sNWs. CO is widely considered as the main poisoning intermediate in EOR, which also mimics the adsorption of $(CH_3CO)_{ads}$ on Pd-based catalysts. We further used CO stripping as a probe model to ascertain the CO tolerance of four catalysts based on the interfacial reaction between adsorbed CO (CO_{ads}) and OH_{ads}. As shown in Fig. 6e, a largest active area of the oxidation peak was achieved for Pd_2Ag_1 sNWs, which was higher than the bimetallic Pd_2Ag_1 pNWs and NPs and Pd NPs. The larger active area of the oxidation peak identified the better CO oxidation activity, and thus kinetically facilitated the removal of poisoning carbonaceous intermediates. The results further indicated that 1D ultrathin PdAg sNWs with single-crystalline feature and high density of low-coordinate atomic steps effectively improved CO anti-poisoning ability and thus enhanced EOR activity. Electrochemical impedance spectra (EIS) was also investigated to understand the charge transfer kinetics in electrocatalytic EOR. As shown in Figure S11, the diameter of impedance arc (DIA), which is decided by charge-transfer resistance, is strongly affected by the catalysts, following an order of single-crystalline Pd_2Ag_1 sNWs < Pd_2Ag_1 NPs ≈ Pd sNWs < Pd NPs. The results indicated that single-crystalline Pd_2Ag_1 sNWs possessed the smallest charge-transfer resistance and faster electrolysis rates for EOR, due to the higher conductivity and acceleration of charge transfer originated from ultrathin 1D single-crystalline nanostructures and bimetallic PdAg alloys.

Electrocatalytic activities of bimetallic PdAg nanoalloys with different compositional ratio of Pd/Ag were also studied for the EOR (Fig. 7a). The electrocatalytic activities of bimetallic PdAg NSs were strongly related to their elemental compositions. A "volcano"-type electrocatalytic mass activity of bimetallic PdAg versus the Pd/Ag ratio was seen, indicating a compositional effect of the catalysts. Among them, ultrathin bimetallic Pd_2Ag_1 sNWs were the optimal electrocatalyst with the best activity for the EOR (Fig. 7b). Meanwhile, in comparison to PdAg NSs with different compositional ratios, bimetallic Pd_2Ag_1 sNWs displayed the lowest onset potential (Fig. 7c), the largest active area of the oxidation peak from CO stripping (Fig. 7d), and the quickest electrocatalytic kinetics, since this material has the lowest activation energy (Figure S12). These results suggest elemental compositional advantages of ultrathin Pd_2Ag_1 sNWs in enhancement for
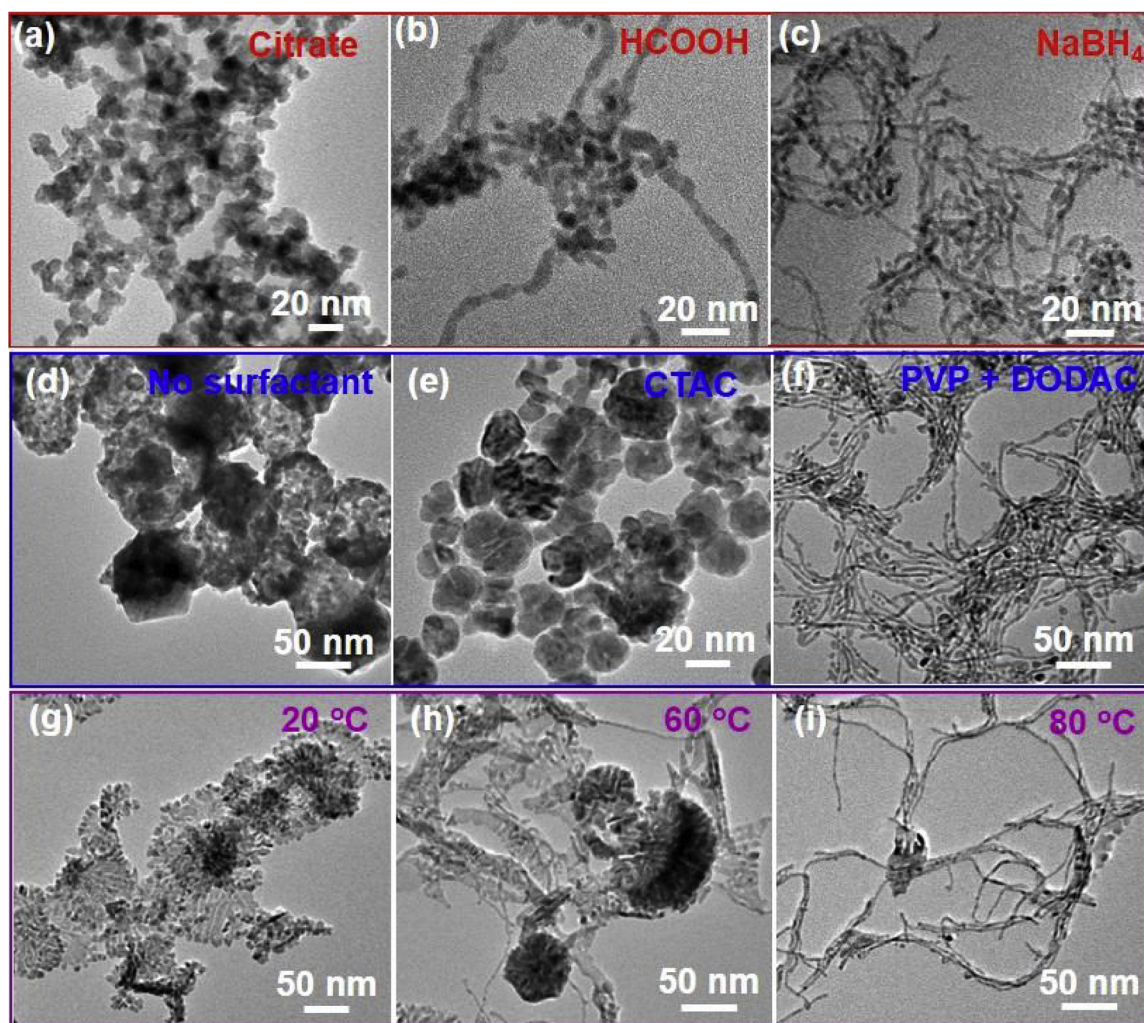
Fig. 5. (a–c) TEM images of the as-resulted Pd_2Ag_1 NCs synthesized with different reducing agent of (a) sodium citrate, (b) formic acid, and (c) $NaBH_4$, (d) without surfactant and with different surfactant of (e) CTAC and (f) PVP/DODAC, in the different temperature of (g) 20 °C, (h) 60 °C and (i) 80 °C.

EOR activity.

The electrocatalytic investigations above strongly suggest that both structural and compositional advantages of ultrathin Pd_2Ag_1 sNWs contribute synergistically to enhance electrochemical EOR activity, through electronic and bifunctional effects. On the one hand, single-crystalline sNWs with ultrathin diameter (3 nm), ultralong length (100–1000 nm) and high density of low-coordinate atomic steps not only structurally increased the utilization efficiency of Pd and exposed more electrocatalytically active sites, but also effectively facilitated the electron and mass transfer during the electrocatalysis (electronic effect). These merits kinetically activated the adsorption and diffusion of the reactants, the removal of the intermediates and products, and thus resulted in the enhanced EOR activity. On the other hand, alloying more oxophilic Ag would make bimetallic Pd_2Ag_1 sNWs with bifunctional properties, in which Ag atoms effectively accelerated the adsorption of OH_{ads} ($Ag-OH_{ads}$), and thus kinetically enhanced the EOR process via prompting reaction between $Pd-(CH_3CO)_{ads}$ and $Ag-OH_{ads}$. Meanwhile, Ag with a larger lattice alloyed in PdAg NWs shifted the D-band center of Pd up, which thermodynamically weakened the adsorption and diffusion of $(CH_3CO)_{ads}$ and $(OH)_{ads}$ and kinetically accelerated the electrocatalytic processes.

Structural and compositional advantages also rendered ultrathin Pd_2Ag_1 sNWs with superior electrochemical self-stability for the EOR, because of the easier mass/electron transfer and prompting oxidation/removal of the carbonaceous poisons. The stability of ultrathin Pd_2Ag_1 sNWs was studied by two methods (Fig. 8). First, we assessed the cycling stability of ultrathin Pd_2Ag_1 sNWs by continuously performing CV cycles at 50 mV s^{-1} (Figure S13). The gradually decreasing ECSAs indicated the loss of electrocatalytic active sites for the EOR. We further normalized the mass activities against the cycle numbers (Fig. 8a). The mass activity of ultrathin Pd_2Ag_1 sNWs mildly decreased during the cycling, in which 1.23 A mg_{Pd}^{-1} in mass activity was retained after 2500 cycles. By contrast, the mass activity of commercial Pd NPs quickly declined from 0.92 A mg_{Pd}^{-1} to 0.27 A mg_{Pd}^{-1} after 2500 cycles (see CV cycles in Figure S14), as reported in previous works. Second, we also carried out current-time (i–t) chronoamperometry measurements at the peak current density for all samples (Fig. 8b). Similarly, a mild loss was observed for ultrathin Pd_2Ag_1 sNWs which still retained 0.57 A mg_{Pd}^{-1} after 2000 s, 1.1 times higher than Pd_2Ag_1 pNWs (0.50 A mg_{Pd}^{-1}), 2.4 times greater than monometallic Pd sNWs (0.24 A mg_{Pd}^{-1}), 13.5 times higher than Pd_2Ag_1 NPs (0.04 A mg_{Pd}^{-1}), and 51.5 times larger than commercialized Pd NPs (0.01 A mg_{Pd}^{-1}). Both significantly enhanced cycling and chronoamperometric stabilities of ultrathin Pd_2Ag_1 sNWs strongly correspond to the results from CO anti-poisoning experiments (Figs. 6 and 7). This further highlights the structural and compositional advantages of ultrathin Pd_2Ag_1 sNWs for electrocatalytic EOR.
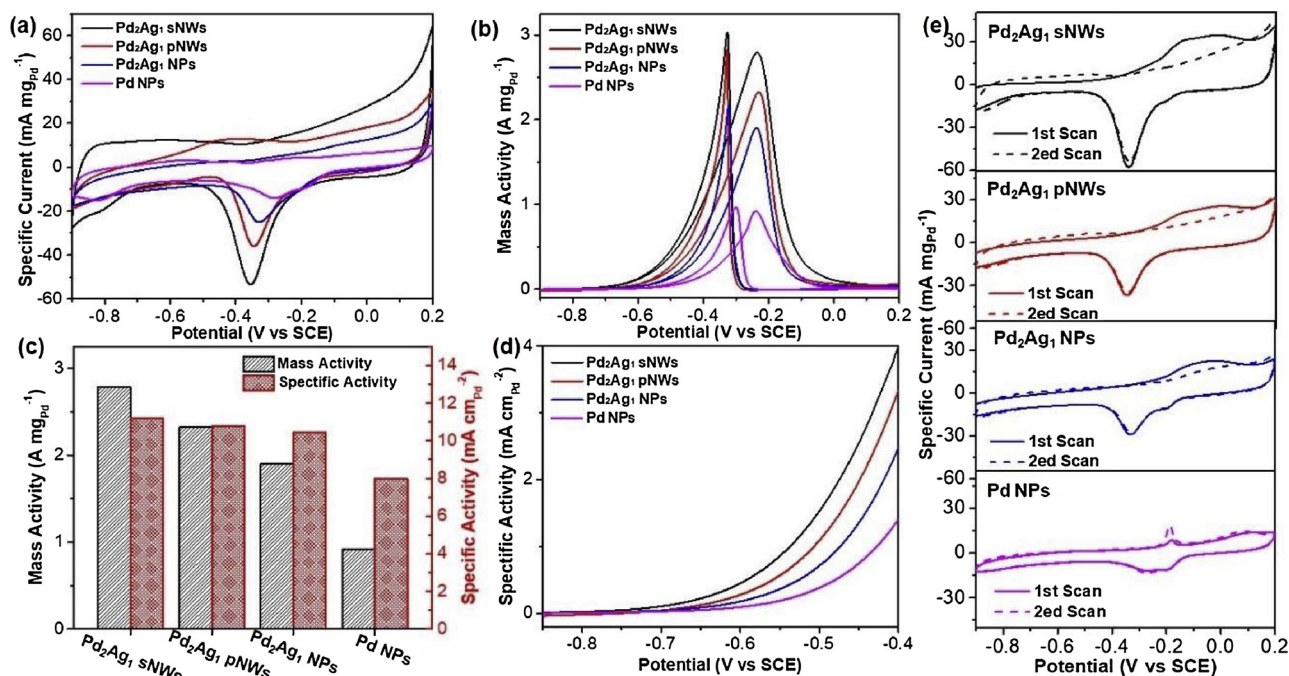
Fig. 6. (a) CV curves of bimetallic Pd$_2$Ag$_1$ sNWs, pNWs and NPs, and commercial Pd NPs in 1.0 M KOH solution with a scan rate of 50 mV s^{-1}. (b) CV curves, (c) summarized mass and specific activities, (d) onset potentials and (e) CO stripping voltammetry of bimetallic Pd$_2$Ag$_1$ sNWs, pNWs and NPs, and commercial Pd NPs in 1.0 M KOH and 1.0 M ethanol with a scan rate of 50 mVs^{-1}. (All above data were collected at 25 °C).

4. Conclusions

In conclusion, we reported a facile and scaled-up solution-phase synthetic strategy to grow in situ highly uniform PdAg NWs with a tunable ratio of Pd/Ag. The resultant PdAg NWs were ultrathin (2.9 nm), ultralong (100–1000 nm), and single-crystalline. Formation mechanism indicated that optimal synthesis conditions were critical for the formation of bimetallic PdAg sNWs. Structural and compositional

advantages of ultrathin Pd$_2$Ag$_1$ sNWs rendered them with enhanced electrochemical EOR activity and stability in alkaline solution (Table S1), compared to their 0D and monometallic counterparts as well as commercial Pd NPs. Kinetic and thermodynamic as well as CO anti-poisoning studies confirmed that synergic electronic and bifunctional effects of single-crystalline PdAg NWs were responsible for the enhanced EOR performances. Our findings offer a feasible, interesting, and very promising viewpoint to boost electrochemical EOR
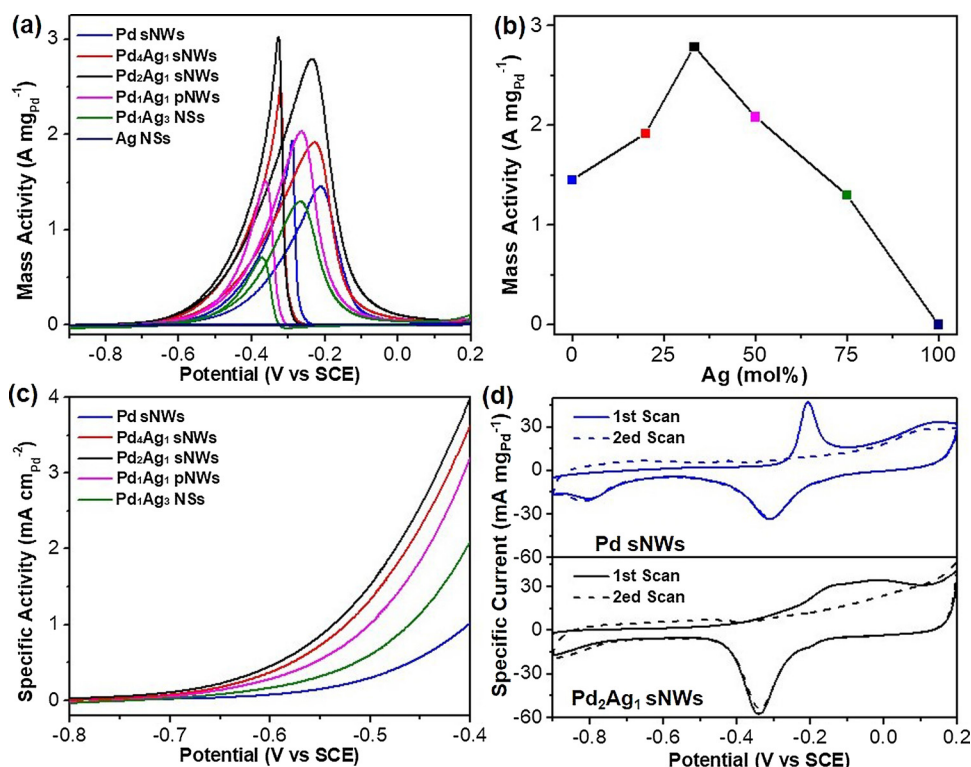

Fig. 7. (a) CV curves, (b) summarized mass activities, (c) onset potentials and (d) CO striping voltammetry of monometallic Pd sNWs and Ag NPs, bimetallic Pd$_4$Ag$_1$ and Pd$_2$Ag$_1$ sNWs, and bimetallic Pd$_1$Ag$_1$ and Pd$_1$Ag$_2$ NSs obtained in 1.0 M KOH and 1.0 M ethanol with a scan rate of 50 mV s^{-1}. (All above data are collected at 25 °C).
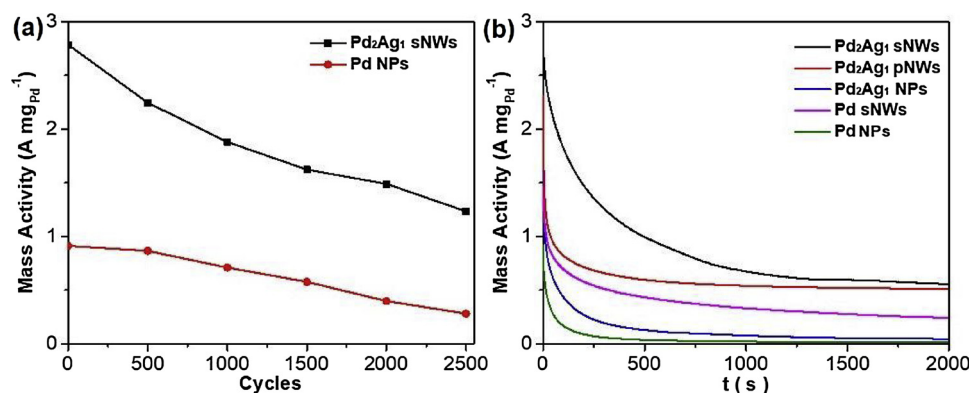
Fig. 8. (a) Electrocatalytic EOR cycling stability curves of ultrathin Pd_2Ag_1 sNWs and Pd NPs, (b) EOR i–t chronoamperometric stability curves of ultrathin Pd_2Ag_1 sNWs, pNWs and NPs, Pd sNWs and NPs.

performance by incorporation of structural (dimension) and compositional (binary/ternary) advantages of multifunctional nanocatalysts.

Conflict of interest

The authors declare no completing financial interest.

Acknowledgments

Appendix A. Supplementary data

Supplementary material related to this article can be found, in the online version, at doi:https://doi.org/10.1016/j.apcatb.2019.02.068.

References

[1] A. Rabis, P. Rodriguez, T.J. Schmidt, Electrocatalysis for polymer electrolyte fuel cells: recent achievements and future challenges, ACS Catal. 2 (2012) 864–890.
[2] E. Antolini, Catalysts for direct ethanol fuel cells, J. Power Sources 170 (2007) 1–12.
[3] M.K. Debe, Electrocatalyst approaches and challenges for automotive fuel cells, Nature 486 (2012) 43.
[4] C. Bianchini, P.K. Shen, Palladium-based electrocatalysts for alcohol oxidation in half cells and in direct alcohol fuel cells, Chem. Rev. 109 (2009) 4183–4206.
[5] A. Chen, C. Ostrom, Palladium-based nanomaterials: synthesis and electrochemical applications, Chem. Rev. 115 (2015) 11999–12044.
[6] Z.X. Liang, T.S. Zhao, J.B. Xu, L.D. Zhu, Mechanism study of the ethanol oxidation reaction on palladium in alkaline media, Electrochim. Acta 54 (2009) 2203–2208.
[7] Y. Yang, L. Jin, B. Liu, P. Kerns, J. He, Direct growth of ultrasmall bimetallic AuPd nanoparticles supported on nitrided carbon towards ethanol electrooxidation, Electrochim. Acta 269 (2018) 441–451.
[8] W. Huang, X. Kang, C. Xu, J. Zhou, J. Deng, Y. Li, S. Cheng, 2D PdAg alloy nanodendrites for enhanced electrooxidation, Adv. Mater. 30 (2018) 1706962.
[9] J.W. Hong, Y. Kim, D.H. Wi, S. Lee, S.U. Lee, Y.W. Lee, S.I. Choi, S.W. Han, Ultrathin free-standing ternary-alloy nanosheets, Angew. Chem. Int. Ed. 55 (2016) 2753–2758.
[10] A.L. Wang, X.J. He, X.F. Lu, H. Xu, Y.X. Tong, G.R. Li, Palladium-cobalt nanotube arrays supported on carbon fiber cloth as high-performance flexible electrocatalysts for ethanol oxidation, Angew. Chem. Int. Ed. 54 (2015) 3669–3673.
[11] L. Chen, L. Lu, H. Zhu, Y. Chen, Y. Huang, Y. Li, L. Wang, Improved ethanol electrooxidation performance by shortening Pd-Ni active site distance in Pd-Ni-P nanocatalysts, Nat. Commun. 8 (2017) 14136.
[12] S. Zhang, Ö. Metin, D. Su, S. Sun, Monodisperse AgPd alloy nanoparticles and their superior catalysis for the dehydrogenation of formic acid, Angew. Chem. Int. Ed. 52 (2013) 3681–3684.
[13] H.-l. Liu, F. Nosheen, X. Wang, Noble metal alloy complex nanostructures: controllable synthesis and their electrochemical property, Chem. Soc. Rev. 44 (2015) 3056–3078.
[14] U.B. Demirci, Theoretical means for searching bimetallic alloys as anode electrocatalysts for direct liquid-feed fuel cells, J. Power Sources 173 (2007) 11–18.
[15] P. Strasser, S. Koh, T. Anniyev, J. Greeley, K. More, C. Yu, Z. Liu, S. Kaya, D. Nordlund, H. Ogasawara, M.F. Toney, A. Nilsson, Lattice-strain control of the activity in dealloyed core–shell fuel cell catalysts, Nat. Chem. 2 (2010) 454–460.
[16] L. Cademartiri, A. Ozin Geoffrey, Ultrathin nanowires-a materials chemistry perspective, Adv. Mater. 21 (2008) 1013–1020.
[17] W. Wang, F. Lv, B. Lei, S. Wan, M. Luo, S. Guo, Tuning nanowires and nanotubes for efficient fuel-cell electrocatalysis, Adv. Mater. 28 (2016) 10117–10141.
[18] Y. Lu, S. Du, R. Steinberger-Wilckens, One-dimensional nanostructured electrocatalysts for polymer electrolyte membrane fuel cells-a review, Appl. Catal. B-Environ. 199 (2016) 292–314.
[19] X. Huang, Z. Zhao, Y. Chen, C.Y. Chiu, L. Ruan, Y. Liu, M. Li, X. Duan, Y. Huang, High density catalytic hot spots in ultrafine wavy nanowires, Nano Lett. 14 (2014) 3887–3894.
[20] Y. Song, R.M. Garcia, R.M. Dorin, H. Wang, Y. Qiu, E.N. Coker, W.A. Steen, J.E. Miller, J.A. Shelnutt, Synthesis of platinum nanowire networks using a soft template, Nano Lett. 7 (2007) 3650–3655.
[21] G. Chen, C. Xu, X. Huang, J. Ye, L. Gu, G. Li, Z. Tang, B. Wu, H. Yang, Z. Zhao, Z. Zhou, G. Fu, N. Zheng, Interfacial electronic effects control the reaction selectivity of platinum catalysts, Nat. Mater. 15 (2016) 564–569.
[22] D. Xu, X. Liu, H. Lv, Y. Liu, S. Zhao, M. Han, J. Bao, J. He, B. Liu, Ultrathin palladium nanosheets with selectively controlled surface facets, Chem. Sci. 9 (2018) 4451–4455.
[23] Z. Liu, J. Qi, M. Liu, S. Zhang, Q. Fan, H. Liu, K. Liu, H. Zheng, Y. Yin, C. Gao, Aqueous synthesis of ultrathin platinum/non-noble metal alloy nanowires for enhanced hydrogen evolution activity, Angew. Chem. 130 (2018) 11852–11856.
[24] Z. Fan, H. Zhang, Template synthesis of noble metal nanocrystals with unusual crystal structures and their catalytic applications, Acc. Chem. Res. 49 (2016) 2841–2850.
[25] C.W. Xu, H. Wang, P.K. Shen, S.P. Jiang, Highly ordered Pd nanowire arrays as effective electrocatalysts for ethanol oxidation in direct alcohol fuel cells, Adv. Mater. 19 (2007) 4256–4259.
[26] H. Huang, K. Li, Z. Chen, L. Luo, Y. Gu, D. Zhang, C. Ma, R. Si, J. Yang, Z. Peng, J. Zeng, Achieving remarkable activity and durability toward oxygen reduction reaction based on ultrathin Rh-doped Pt nanowires, J. Am. Chem. Soc. 139 (2017) 8152–8159.
[27] H. Lv, Y. Chen, D. Xu, Y. Hu, H. Zheng, S.L. Suib, B. Liu, Ultrathin PdPt bimetallic nanowires with enhanced electrocatalytic performance for hydrogen evolution reaction, Appl. Catal. B-Environ. 238 (2018) 525–532.
[28] B.Y. Xia, W.T. Ng, H.B. Wu, X. Wang, X.W. Lou, Self-supported interconnected Pt nanoassemblies as highly stable electrocatalysts for low-temperature fuel cells, Angew. Chem. 124 (2012) 7325–7328.
[29] Z. Chen, M. Waje, W. Li, Y. Yan, Supportless Pt and PtPd nanotubes as electrocatalysts for oxygen-reduction reactions, Angew. Chem. Int. Ed. 46 (2007) 4060–4063.
[30] L. Bu, S. Guo, X. Zhang, X. Shen, D. Su, G. Lu, X. Zhu, J. Yao, J. Guo, X. Huang, Surface engineering of hierarchical platinum-cobalt nanowires for efficient electrocatalysis, Nat. Commun. 7 (2016) 11850.
[31] Y. Kuang, Y. Zhang, Z. Cai, G. Feng, Y. Jiang, C. Jin, J. Luo, X. Sun, Single-crystalline dendritic bimetallic and multimetallic nanocubes, Chem. Sci. 6 (2015) 7122–7129.
[32] M. Luo, Y. Sun, X. Zhang, Y. Qin, M. Li, Y. Li, C. Li, Y. Yang, L. Wang, P. Gao, Stable high-index faceted Pt skin on zigzag-like ptfe nanowires enhances oxygen reduction catalysis, Adv. Mater. 30 (2018) 1705515.
[33] C. Koenigsmann, W.P. Zhou, R.R. Adzic, E. Sutter, S.S. Wong, Size-dependent enhancement of electrocatalytic performance in relatively defect-free, processed ultrathin platinum nanowires, Nano Lett. 10 (2010) 2806–2811.
[34] H. Lv, A. Lopes, D. Xu, B. Liu, Multimetallic hollow mesoporous nanospheres with synergistically structural and compositional effects for highly efficient ethanol electrooxidation, ACS Cent. Sci. 4 (2018) 1412–1419.
[35] D. Bin, B. Yang, K. Zhang, C. Wang, J. Wang, J. Zhong, Y. Feng, J. Guo, Y. Du,

Design of PdAg hollow nanoflowers through galvanic replacement and their application for ethanol electrooxidation, Chem. Eur. J. 22 (2016) 16642–16647.

[36] S. Fu, C. Zhu, D. Du, Y. Lin, Facile one-step synthesis of three-dimensional Pd-Ag bimetallic alloy networks and their electrocatalytic activity toward ethanol oxidation, ACS Appl. Mater. Interfaces 7 (2015) 13842–13848.

[37] B. Wiley, Y. Sun, B. Mayers, Y. Xia, Shape-controlled synthesis of metal nanostructures: the case of silver, Chem. Eur. J. 11 (2004) 454–463.

[38] Q. Zhang, Y. Hu, S. Guo, J. Goebl, Y. Yin, Seeded growth of uniform Ag nanoplates with high aspect ratio and widely tunable surface plasmon bands, Nano Lett. 10 (2010) 5037–5042.

[39] D. Xu, X. Liu, M. Han, J. Bao, Facile synthesis of ultrathin single-crystalline palladium nanowires with enhanced electrocatalytic activities, Chem. Commun. 52 (2016) 12996–12999.

[40] Y.W. Lee, M. Kim, S.W. Kang, S.W. Han, Polyhedral bimetallic alloy nanocrystals exclusively bound by {110} facets: Au-Pd rhombic dodecahedra, Angew. Chem. 123 (2011) 3528–3532.

[41] Y. Jia, Y. Jiang, J. Zhang, L. Zhang, Q. Chen, Z. Xie, L. Zheng, Unique excavated rhombic dodecahedral PtCu3 alloy nanocrystals constructed with ultrathin nanosheets of high-energy {110} facets, J. Am. Chem. Soc. 136 (2014) 3748–3751.

[42] E. Feitosa, P.C.A. Barreleiro, G. Olofsson, Phase transition in dioctadecyldimethylammonium bromide and chloride vesicles prepared by different methods, Chem. Phys. Lipids 105 (2000) 201–213.

[43] R.G. Laughlin, R.L. Munyon, Y.C. Fu, A.J. Fehl, Physical science of the dioctadecyldimethylammonium chloride-water system. 1. Equilibrium phase behavior, J. Phys. Chem. 94 (1990) 2546–2552.

[44] S.T. Nguyen, H.M. Law, H.T. Nguyen, N. Kristian, S. Wang, S.H. Chan, X. Wang, Enhancement effect of ag for Pd/C towards the ethanol electro-oxidation in alkaline media, Appl. Catal. B-Environ. 91 (2009) 507–515.

[45] C. Peng, Y. Hu, M. Liu, Y. Zheng, Hollow raspberry-like PdAg alloy nanospheres: high electrocatalytic activity for ethanol oxidation in alkaline media, J. Power Sources 278 (2015) 69–75.